# The Effect of Surface Flaws on Nanosecond Shock Wave Induced Brittle Fracture

by

Junqin Chen

Department of Mechanical Engineering and Material Science
Duke University

Date:_____

Approved:

_____
Pei Zhong, Advisor

_____
John Dolbow

_____
Donald Bliss

_____
George Delagrammatikas

Thesis submitted in partial fulfillment of
the requirements for the degree of
Master of Science in the Department of
Mechanical Engineering and
Materials Science in the
Graduate School of
Duke University

2020

ABSTRACT

The Effect of Surface Flaws on Nanosecond Shock Wave Induced Brittle Fracture

by

Junqin Chen

Department of Mechanical Engineering and Materials Science
Duke University

Date:_____
Approved:

_____
Pei Zhong, Advisor

_____
John Dolbow

_____
Donald Bliss

_____
George Delagrammatikas

An abstract of a thesis submitted in partial
fulfillment of the requirements for the degree
of Master of Science in the Department of
Mechanical Engineering and
Materials Science in the
Graduate School of
Duke University

2020

## Abstract

Nano pulse lithotripsy (NPL) is a novel medical technology to fragment urinary calculi through electrical discharge. Compared with traditional shock wave lithotripters utilizing focused shock waves, NPL is ideal for investigating the stress field induced by surface acoustic waves (SAWs), such as the leaky Raleigh waves (LRWs), on the fluid-solid boundary. A pioneering study has recently demonstrated the generation of LRWs induced by the spherically divergent shock wave at the borosilicate glass-water boundary in NPL treatment. The resultant tensile stress field was found to play an important role in the initiation of cracks and the formation of ring-like fracture on the glass surfaces. This prior work motivates us to investigate the effect of SAWs on surface flaws that can be artificially and controllably created on the glass surface by microindentations to mimic the surface erosion induced by cavitation. In this study, we used a microhardness tester with a Vickers indenter and applied a load of 1.0 kg with a dwell time of 10 s to produce indentations at various radial distances (1.0 mm, 1.5 mm, 2.0 mm and 2.5 mm) on the borosilicate glass samples (50 x 50 x 3.3 mm in LxWxH). Each indentation creates a pyramid shaped impression with an average diagonal length of 55 μm and penetration depth of 7.8 μm. At a standoff distance of 1.5 mm, the shock waves generated by the NPL probe were applied to the glass surface until the glass was broken. After each shock impact, the crack initiation and extension around each

indentation site were recorded, from which the speed of crack development represented by the arc length per shock was calculated. Through these experiments, we have made the following important observations. First, the artificially induced surface flaws made by the microindentation can well control the location of the crack initiation since the presence of surface flaws will significantly weaken the glass surface. Under the effect of the maximum tensile stress ($\sigma_{T,max}$) generated by NPL shock wave impact, the cracks extending from the indentation impression site are predominantly aligned perpendicular to the direction of LRWs (which is also the direction of $\sigma_{T,max}$). Second, compared with the number of shocks required to initiate the ring-like fracture on the original (untreated) glass surface, fewer shock waves are needed to initiate the ring-like crack formation and extension from the impression site presumably due to the higher stress concentration built up at the tip of the surface flaws during NPL, which can greatly reduce the tensile stress or stress integral required to initiate a crack. The average speed of ring-like fracture formation at a radial distance about 1.5 mm is 0.26 mm per shock on the glass without microindentations. By contrast, the average speed of crack extension at the same radial distance with microindentations can increase to 0.34 mm per shock. Furthermore, the speed of crack extension varies with the radial distance of the microindentation from the NPL probe axis, largely following the variation of the local tensile stress integral generated by the LRWs. Altogether, these findings suggest potential synergy between shock wave-induced LRWs and surface flaws (e.g., produced

by cavitation erosion pitting during shock wave lithotripsy) that may lead to improved stone comminution, which warrants future investigations.

# Contents

# List of Tables

# List of Figures

## Acknowledgements

I would like to take this opportunity to express the deepest gratitude to my research supervisor, Dr. Pei Zhong, for his encouragement to pursue this project, for his every prompt and important suggestion, and for his sincere support. His patience, diligence, erudition, and unique insights into the field of shock wave lithotripsy kept me constantly engaged with my research. It is my honor to meet such a mentor in my academic career.

I would like to acknowledge Yiying Huang and Shaopeng Zhang for their contributions in literature review, experimental setup, and data collection at the beginning of this study. Without them, this study cannot run so smoothly. I would like to express my sincere gratitude to all the staff in the MEMS department and members of Zhong Lab for their technical supports and useful advices.

My sincere appreciation also goes to my parents, Ying Chen and Jianjun Chen, for their unconditional love without expecting any return. During my past six-year college and graduate studies in the U.S., persistence and enthusiasm about life are the most precious things they taught me. Finally, I would like to thank my boyfriend, Yuan Wei, for his accompanying in my toughest moments and his supporting to every decision I made.

# 1. Introduction

## *1.1 Nano pulse lithotripsy (NPL)*

Nano Pulse lithotripsy (NPL) is a novel intracorporeal technology that utilizes nanosecond duration electric pulses transmitted through a flexible coaxial probe to break up kidney stones in the urinary tract. Under the guidance of a ureteroscope, NPL can deliver a spark discharge at 10 kV of 250 - 500 ns duration to fragment the target stone with high efficiency. For example, when treating a 6 mm soft BegoStone cylindrical phantom (Powder to water ratio: 5:2), the stone fragmentation efficiency using a 3.6 Fr NPL probe can reach 173 mg/min (Kaplan et al., 2016).

Compared with traditional shock wave lithotripters (electrohydraulic, electromagnetic and piezoelectric), the mechanisms of stone comminution in NPL consist of shock wave, cavitation, and possible dielectric breakdown near the probe tip (Kaplan et al., 2016). Recent studies based on a comparison between experimental results and the stress field analysis in mathematical modeling, the collapse of cavitation bubbles produced by NPL may have minimal effects on the initiation and formation of cracks and stone damage produced on BegoStone phantoms (Yang, 2017).

## *1.2 Surface acoustic waves (SAWs) in NPL*

In shock wave lithotripsy (SWL), stone comminution is considered as a dynamic process consisting of two distinctly different stages. One is the early accelerating stage

caused primarily by the stress field and the other is the late decelerating state, in which cavitation, surface acoustic waves (SAWs), and their potential synergistic interactions have been proposed as a critical mechanism of stone fragmentation (Zhong, 2013). Using numerical simulations, it has also been demonstrated that during shock wave interaction with both cylindrical and spherical stone phantoms, shear waves and SAWs could be generated at the fluid-solid boundary (Cleveland & Sapozhnikov, 2005). In addition, under the treatment of highly focused shock waves, a ring-like fracture pattern was detected experimentally on the surface of thin slabs of artificial Plaster-of-Paris stone phantoms. This specific fracture was hypothesized to be generated by the interaction of the reflected longitudinal waves and SAWs during the treatment (Zhong, 2013).

In a recent study, a similar ring-like fracture was detected on the glass surface under the treatment of a nanosecond spark-generated shock wave. The leaky Raleigh wave (LRW), which is a special type of SAWs, was proposed to drive the initiation and extension of the ring-like fracture both experimentally and numerically (Zhang, Yang & Zhong, 2019).

## *1.3 Cavitation in stone fragmentation during SWL*

Cavitation-induced damage was considered as another important mechanism that contributes to the stone fragmentation in SWL. In 1986, Andrew Coleman and colleagues used an extracorporeal shockwave lithotripter (ESWL) to treat the target

surface (x-ray film, thin aluminum sheets and metal plates). They observed that the liquid jet impacts induced by the asymmetric bubble collapse near a solid boundary could generate deep depressions throughout >200 $cm^3$ volume on the aluminum foil with 0.02 mm thickness as shown in Figure 1(a) and 1(b) (Coleman et al., 1987). When a cylindrical U-30 artificial stone was treated by 50 shock waves using an HM3 lithotripter, numerous individual bubbles were observed to form bubble clusters at two ends of the stone and on the side surfaces. A 2 mm diameter crater finally formed at the center of the proximal end (Pishchalnikov et al., 2003). Moreover, it has been shown that when Plaster-of-Paris stone phantoms were exposed to shock waves produced by an HM-3 lithotripter in castor oil, which can suppress cavitation with influencing the transmission of the shock waves, only 11% of fragments are clinically passable (< 2 mm) after 500 shocks. By contrast, clinically passable fragments produced in partially degassed water can reach to 66% after the same treatment. These findings clearly demonstrated the important role of cavitation in the success of SWL. It was also proposed that cavitation with jetting from collapsing bubble near a stone surface could lead to surface erosion, and furthermore, bubble expansion in the pitting might also produce large tensile stress to facilitate crack extension as demonstrated in Figure 1(c) (Zhu, Cocks, Preminger & Zhong, 2002).

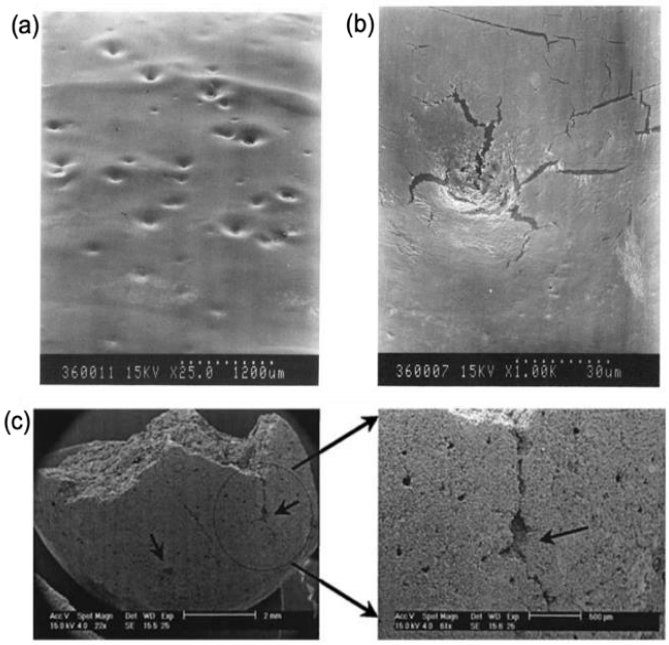


**Figure 1: (a) A general view of depressions on the aluminum foil (0.02 mm thickness)exposed to the shock waves generated by ESWL under a scanning electron microscope; (b) Closer view of a single depression (Coleman et al., 1987); (c) A deep pitting on the surface of a Plaster-of-Paris stone fragment with radial cracks (Zhu et al., 2002)**

## *1.4 Motivation of creating artificial surface flaws*

However, due to the irregular shape of the surface erosion on the artificial kidney stones, limited evidence has demonstrated the direct influence of SAWs on the crack development from surface flaws induced by cavitation. To gain insight into the damage mechanism, most previous studies conducted experiments using brittle materials with smooth and flat surfaces and well characterized material properties. For example, Bowden, Philip, and Field used liquid jets to apply explosive loading to the

surface of a fixed glass plate in air where randomly distributed pre-existing flaws were present. They concluded that the opening and closing of fractures were caused by the interaction of surface waves (i.e., Rayleigh waves) and reflected longitudinal waves produced by the liquid droplet impact (Bowden, Philip & Field, 1964). Another study used pulsed laser radiation to generate nonlinear SAW pulses with shock formation in fused quartz and silicon samples, and found that a single laser pulse could produce a series of cracks extending in the direction perpendicular to the SAW propagation (Lomonosov & Hess, 2002). In addition, surface wave methods have been well developed to detect the surface breaking cracks (Buck, Thompson, & Rehbein, 1988). Most previous studies investigated the initiation and development of cracks from intrinsic flaws on the surface and neglected the effect of extrinsic surface flaws, induced for example by cavitation erosion, on the initiation and extension of the cracks by SAWs.

In order to conduct a well-controlled and reproducible experiment, borosilicate glass was chosen because it is a common material available at regular shape and size. Due to the transparency of the glass, the crack formation on its surface can be easily detected and recorded. Also, the borosilicate glass has similar density, acoustic wave speeds and impedances to the corresponding values of human kidney stones (Zhong, Chuong & Preminger, 1993). As shown in Table 1, the density of the borosilicate glass is

close to the real kidney stones; its longitudinal and transverse wave speed is a little higher.

**Table 1: Density and acoustic wave speeds of renal calculi and borosilicate glass**

| Material | Density ($kg/m^3$) | Longitudinal wave speed (m/s) | Transverse wave speed (m/s) |
|---|---|---|---|
| COM (100) | 2038 ± 34 | 4535 ± 58 | 2132 ± 25 |
| Brushite (95)/COM (5) | 2157 ± 16 | 3932 ± 134 | 1820 ± 22 |
| Uric Acid (100) | 1546 ± 12 | 3471 ± 62 | 1464 ± 12 |
| **Borosilicate Glass** | **2230** | **5587** | **3454** |

To mimic surface flaws induced by cavitation, a microhardness tester with Vickers indenter was employed to create well-defined indentation impressions on the glass surface. Normally, Vickers hardness testing is performed to measure the microhardness of a material. For an isotropic and homogenous material, the shape of indentations will be a square-based pyramid with consistent diagonal lengths (Sehgal & Ito, 1999), as shown in Figure 2(b).

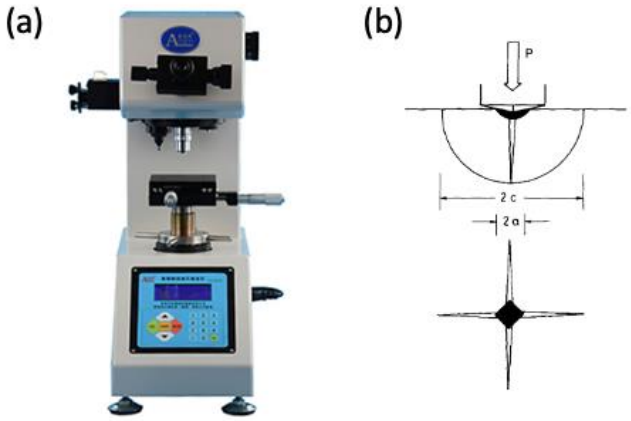


**Figure 2: (a) Microhardness tester (HV-1000, AICEYI); (b) A schematic diagram of the indentation created by Vickers indenter (Anstis et al., 1981)**

## *1.5 Aims and content of the thesis*

In this study, we aim to address two main limitations in the previous studies: (i) no spatially localized dynamic fracture processes have been studied using well-defined artificially induced surface flaws in SWL, and (ii) no quantitative correlation has been carried out between the SAWs generated by shock waves and the resultant extension and propagation characteristics of the artificially induced surface cracks. The relevant theoretical background will be introduced in Chapter 2.

We used NPL probe to conduct experiments on the glass surface without and with microindentations at different radial distances from the focal point (i.e., the

projection center of the probe axis on the glass surface). Under a fixed standoff distance of 1.5 mm, the pulse energy delivered by the NPL probe was well controlled within a given range of the probe lifespan. The details of experimental setup and the selection of optimal lifespan, standoff distance, locations of microindentations will be presented in Chapter 3. In Chapter 4, the crack extension and propagation characteristics from the microindentation sites will be first separated into two groups: 1) crack extension along the direction of SAWs propagation and 2) crack extension in the direction perpendicular to SAWs propagation. The comparison of the results between these two groups allows us to investigate the effect of NPL-induced stress field at the water-glass boundary. Next, the arc length of circumferential cracks initiated from different microindentation sites will be compared to determine how the strength of the SAWs would affect crack extension at various radial distances from the focal point. Finally, the overall processes of the crack formation, extension and fracture on the glass surface with and without microindentations will be compared. The speed of crack extension will be presented in Chapter 5 to demonstrate the effect of artificially induced surface flaws on the crack extension speed and fracture on the borosilicate glass surface.

# 2. Theoretical background

## *2.1 Modes of elastic wave propagation in solids*

When a lithotripter shock wave (LSW) impinges on the surface of an isotropic and homogeneous elastic medium, i.e., borosilicate glass in this study, the dilatational displacement of the medium is attributed to the disturbance induced by a longitudinal (or P) wave and the rotational displacement is caused by a transvers (or S) wave (Zhong, 2013).

The Cauchy-Navier equation of motion in an isotropic linear elastic solid is given by (Sokolnikoff, 1956):

$$(\lambda + \mu)\nabla(\nabla \cdot u) + \mu\nabla^2 u = \rho\frac{\partial^2 u}{\partial^2 t} \tag{2.1}$$

where u is the displacement in the material. Eqn. (2.1) can be re-written for harmonic motions in the form of wave equations for the two elastic waves with $c_l$ representing P wave speed and $c_t$ representing S wave speed, respectively,

$$\nabla^2\Phi - \frac{1}{c_l^2}\frac{\partial^2\Phi}{\partial^2 t} = 0, c_l = \sqrt{\frac{\lambda + 2\mu}{\rho}} \tag{2.2}$$

$$\nabla^2\Psi - \frac{1}{c_t^2}\frac{\partial^2\Psi}{\partial^2 t} = 0, c_t = \sqrt{\frac{\mu}{\rho}} \tag{2.3}$$

where $\lambda$ and $\mu$ are the Lame coefficients; $\rho$ is the density of the solid; $\Phi$ and $\Psi$ are the scalar and vector potentials used to express u by the Helmholtz's theorem ($u = \nabla\Phi + \nabla \times \Psi$).

The solutions of Eqn. (2.2) and (2.3) are in the form of

$$\Phi = \Phi(x, y, z)e^{-i\omega t} \tag{2.4}$$

$$\Psi = \Psi(x, y, z)e^{-i\omega t} \tag{2.5}$$

for a harmonic motion in a Cartesian coordinate system, where $\omega$ is the angular frequency. By substituting (2.4) and (2.5) into (2.2) and (2.3), we can finally obtain a time-independent form of the wave equation,

$$\nabla^2\Phi - k_l^2\Phi = 0,\ k_l = \frac{\omega}{C_l} \tag{2.6}$$

$$\nabla^2\Psi - k_t^2\Psi = 0,\ k_t = \frac{\omega}{C_t} \tag{2.7}$$

where $k_l$ and $k_t$ are the wave numbers of the longitudinal and transversal waves in the solid.

Besides P and S waves, surface waves including leaky Raleigh waves (LRW) and Scholte waves can be generated at the fluid-solid boundary. In 1952, Schoch investigated the reflection of a bounded ultrasonic beam from a liquid-solid interface and pointed out that the reflected beam was displaced laterally from the position when the angle of incidence satisfied the equation (Schoch, 1952):

$$\sin\theta_R = \frac{c_i}{c_R} \tag{2.8}$$

where $c_i$ is the sound speed in the fluid, $\theta_R$ is now known as the Rayleigh angle and $c_R$ is the Raleigh wave speed on the solid boundary.

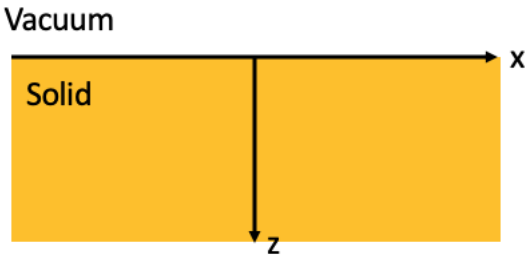


**Figure 3: The coordinate system of the vacuum-solid boundary**

Figure 3 shows the coordinate system applied to analyze Rayleigh wave scattering at the vacuum-solid boundary. The Rayleigh wave propagates along the positive direction of the x-axis with the amplitude depending only on z. Therefore, the scalar and vector potentials of the Rayleigh wave can be written as

$$\Phi(\mathrm{x},\mathrm{z},\mathrm{t}) = \mathrm{F}(z)e^{i(k_R x-\omega t)} \tag{2.9}$$

$$\Psi(\mathrm{x},\mathrm{z},\mathrm{t}) = G(z)e^{i(k_R x-\omega t)} \tag{2.10}$$

where $k_R$ represents the x-component of the Raleigh wave number.

By substituting (2.9) and (2.10) into (2.6) and (2.7), we can obtain two linear differential equations regarding $\mathrm{F}(z)$ and $\mathrm{G}(z)$:

$$\frac{\partial^2 F(z)}{\partial y^2} = \left({k_R}^2 - k_l^2\right)F(z) \tag{2.11}$$

$$\frac{\partial^2 F(z)}{\partial y^2} = \left({k_R}^2 - k_l^2\right)F(z) \tag{2.12}$$

Since the wave is decreasing exponentially as a function of z, the final equations of Φ and Ψ for the Raleigh wave become

$$\Phi(\mathrm{x}, \mathrm{z}, \mathrm{t}) = Ae^{-\sqrt{{k_R}^2 - k_l^2}z + i(k_R x - \omega t)} \tag{2.13}$$

$$\Psi(\mathrm{x}, \mathrm{z}, \mathrm{t}) = Be^{-\sqrt{{k_R}^2 - k_t^2}z + i(k_R x - \omega t)} \tag{2.14}$$

where A and B are arbitrary constants. By using the Hook's law in elastic solids:

$$\sigma_{ij} = a_{ijkl}\epsilon_{kl} \tag{2.15}$$

where the stress components are given by:

$$\sigma_{xx} = \lambda\left(\frac{\partial^2 \Phi}{\partial x^2} + \frac{\partial^2 \Phi}{\partial z^2}\right) + 2\mu\left(\frac{\partial^2 \Phi}{\partial x^2} - \frac{\partial^2 \Psi}{\partial x \partial z}\right) \tag{2.16}$$

$$\sigma_{zz} = \lambda\left(\frac{\partial^2 \Phi}{\partial x^2} + \frac{\partial^2 \Phi}{\partial z^2}\right) + 2\mu\left(\frac{\partial^2 \Phi}{\partial z^2} + \frac{\partial^2 \Psi}{\partial x \partial z}\right) \tag{2.17}$$

$$\sigma_{xz} = \mu\left(\frac{\partial^2 \Psi}{\partial x^2} - \frac{\partial^2 \Psi}{\partial z^2} + 2\frac{\partial^2 \Phi}{\partial x \partial z}\right) \tag{2.18}$$

By combining equations 2.13-18 with the boundary condition: $\sigma_{zz}(x, 0, t) = \sigma_{xz}(x, 0, t) = 0$, two equations containing the arbitrary constants A and B can be obtained as:

$$\begin{cases} k_R^2 \dfrac{\lambda}{2\mu} A - \left(k_R^2 - k_l^2\right)\left(1 + \dfrac{\lambda}{2\mu}\right) A + ik_R \sqrt{{k_R}^2 - k_t^2}\, B = 0 \\ 2ik_R \sqrt{{k_R}^2 - k_l^2}\, A + (2k_R^2 - k_t^2) B = 0 \end{cases} \tag{2.19}$$

The non-trivial solutions of eq. (2.19) lead to the condition:

$$4k_R^2 \sqrt{{k_R}^2 - k_t^2} \sqrt{{k_R}^2 - k_l^2} - (2k_R^2 - k_t^2)^2 = 0 \tag{2.20}$$

which has the polynomial form:

$$\eta^6 - 8\eta^4 + 8(3 - 2\xi^2)\eta^2 - 16(1 - \xi^2) = 0 \tag{2.21}$$

where $\eta = \frac{k_t}{k_R}$ and $\xi = \frac{k_l}{k_t}$. Equation (2.21) is known as the Rayleigh wave equation (Raleigh, 1887), which has six roots. It has been shown that the Raleigh wave equation has only one solution for $k_R$ that is always real (Nkemzi, 1996) and larger than $k_t$. Since $k_R$>$k_t$>$k_l$, thus we have $c_R$<$c_t$<$c_l$. From (2.13) and (2.14), it can also be concluded that the longitudinal and transversal mode of the Raleigh wave penetrates into the solid at a decay rate of $e^{-\sqrt{{k_R}^2 - k_l^2}}$ and $e^{-\sqrt{{k_R}^2 - k_t^2}}$, respectively.

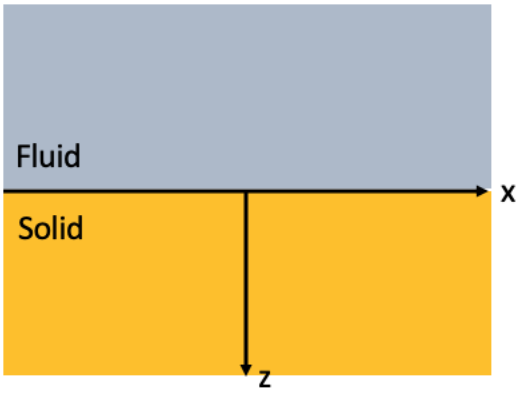


**Figure 4: The coordinate system of the fluid-solid boundary**

Now, let us consider an inviscid fluid-solid boundary as shown in Figure 4. The displacement potential of the fluid still satisfies the wave equation

$$\nabla^2\varphi - \frac{1}{c_o^2}\frac{\partial^2\varphi}{\partial^2 t} = 0 \tag{2.22}$$

which has a general solution with the form of

$$\varphi(x,z,t) = Ce^{i(kx-hz-\omega t)} \tag{2.23}$$

where $k^2 + h^2 = k_0^2$ and $k_0 = \frac{\omega}{c_0}$, $c_0$ is the sound speed in the fluid. The stress components of the solid still satisfy Eqn. (2.16)-(2.18) but the boundary conditions become

$$w_o = w \tag{2.24}$$

$$\sigma_{zz}(x,0,t) = -p \tag{2.25}$$

$$\sigma_{xz}(x, 0, t) = 0 \tag{2.26}$$

where $w_o$ is the displacement of the fluid in the z-direction and p is the pressure in the fluid. Combining these boundary conditions, stress components, and potential displacements together, we can obtain a new characteristic equation for k:

$$\eta'^6 - 8\eta'^4 + 8\left(3 - 2\xi'^2\right)\eta'^2 - 16\left(1 - \xi'^2\right) = i\frac{\rho_0}{\rho}\frac{\sqrt{1 - \xi'}}{\sqrt{\frac{k_o}{k} - \eta'^2}}k_t^4 \tag{2.27}$$

where $\eta' = \frac{k_t}{k}$, $\xi' = \frac{k_l}{k_t}$, and $\rho_0$ is the density of the fluid. A complex root of this equation which has the real part larger than $k_l$ and smaller than $k_t$, can be regarded as the wave number ($k_{LRW}$) of the leaky Raleigh wave. The leaky Rayleigh wave exists in the solid only if $c_t > c_0$. By inspecting the final solutions of Φ and Ψ for the Leaky Raleigh wave:

$$\Phi(\mathrm{x}, \mathrm{z}, \mathrm{t}) = Ae^{-\sqrt{{k_{LRW}}^2 - k_l^2}z + i(k_{LRW}x - \omega t)} \tag{2.28}$$

$$\Psi(\mathrm{x}, \mathrm{z}, \mathrm{t}) = iA\frac{2k_{LRW}\sqrt{k_{LRW}^2 - k_l^2}}{2k_{LRW}^2 - k_t^2}k_t^4 e^{-\sqrt{{k_{LRW}}^2 - k_t^2}z + i(k_{LRW}x - \omega t)} \tag{2.29}$$

it can be concluded that the leaky Raleigh wave also attenuates exponentially into the solid by the rates of $e^{-\sqrt{{k_{LRW}}^2 - k_l^2}}$ and $e^{-\sqrt{{k_{LRW}}^2 - k_t^2}}$. Most energy of the leaky Raleigh wave resides in the solid (Zhu & Popovics, 2006). A unique real root of the characteristic equation (2.27) is the wave number of another type of SAWs, which is known as Scholte wave. The speed of the Scholte wave is smaller than $c_0$ and the energy of the Scholte

wave is localized primarily in the fluid (Guesev et al., 1996). The leaky Rayleigh wave fronts can be separated from the subsequent Scholte wave at large radial distances (Zhu & Popovics, 2006).

## *2.2 Interaction between SAWs and surface cracks*

The surface acoustic wave is commonly used to detect surface defects and determine the size of surface flaws. During the 1980s, Khuri and his colleagues used a low frequency scattering model to study the indentation-induced residual stress on crack extension and predict the size of surface cracks in ceramics (Khuri-Yakub et al., 1980). In addition, another research group applied ultrasonic surface acoustic waves to measure the depths of small cracks in 7075-T651 aluminum and 4340 steel (Yuce, Nelson & Resch, 1985).

A theoretical study on a homogeneous, isotropic, and elastic half-plane with a crack of depth d normal to the solid surface, which is shown in Figure 5, derived the formula of crack-opening displacements.

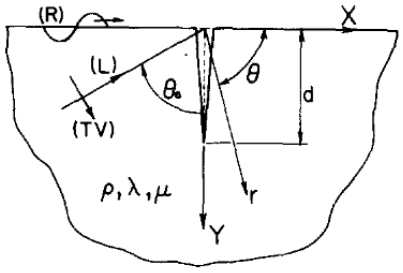


**Figure 5: A two-dimensional geometry containing a normal edge crack (Mendelsohn et al., 1980)**

A Raleigh surface waves originating from $x = -\infty$ and $y = 0$ can induce the incident displacement field:

$$u(X,Y) = A[e^{-(k_R^2-k^2)^{\frac{1}{2}}KY} - \frac{2k_R^2}{2k_R^2-k^2}e^{-(k_R^2-1)^{\frac{1}{2}}KY}]e^{ik_R{}^{KX}} \tag{2.30}$$

$$v(X,Y) = Ai[\frac{k_R}{(k_R^2-k^2)^{\frac{1}{2}}}e^{-(k_R^2-k^2)^{\frac{1}{2}}KY} - \frac{2(k_R^2-1)^{\frac{1}{2}}}{2k_R^2-k^2}e^{-(k_R^2-1)^{\frac{1}{2}}KY}]e^{-ik_R{}^{KX}} \tag{2.31}$$

where $k = \frac{c_l}{c_t}$. The stress field in the Y direction was calculated by

$$\tau_x(0,Y) = 2i\mu k_R K(\frac{A}{d})[e^{-(k_R^2-k^2)^{\frac{1}{2}}KY} - \frac{2k_R^2-2+k^2}{2k_R^2-k^2}e^{-(k_R^2-1)^{\frac{1}{2}}KY}] \tag{2.32}$$

$$\tau_{xy}(0,Y) = \mu K(\frac{A}{d})\frac{2k_R^2-k^2}{(k_R^2-k^2)^{\frac{1}{2}}}[e^{-(k_R^2-1)^{\frac{1}{2}}KY} - e^{-(k_R^2-k^2)^{\frac{1}{2}}KY}] \tag{2.33}$$

where $K = k_l d$, and d is the depth of the crack. Then both horizontal and vertical displacements of the forward- and back-scattered surface waves were calculated at the points (10d, 0) and (-10d, 0), respectively and plotted versus the dimensionless frequency. The differences between the approximated values and the exact solutions of

the back-scattered surface waves suggests that the surface motions are more dominant in the scattered field ahead of the crack than back of the crack (Mendelsohn et al., 1980).

## 2.3 Basic concepts of fracture mechanics

Three fundamental modes of fracture exist in brittle materials, including: Mode I, opening mode driven by the applied tensile stress loading perpendicular to the crack surface; Mode II, sliding mode referring to the shear stress applied perpendicular to the leading edge of a crack and parallel to the crack plane; Mode III, tearing mode driven by the applied shear stress out of plane, which is parallel to both crack plane and crack front.

The first successful theoretical analysis of fracture in brittle materials was introduced by Griffith. His study showed that the fracture strength largely depended on the crack length, which can be demonstrated by the following equation (Griffith, 1921):

$$\sigma_f \sqrt{a} = \sqrt{\frac{2E\gamma}{\pi}} \tag{2.34}$$

where $\sigma_f$ is the tensile stress that leads to fracture, a is the crack length, E is Young's modulus of the material, and $\gamma$ is the surface energy density. Griffith's work was initially ignored by his contemporaries due to the fact that the energy required to cause fracture is often much higher than the corresponding surface energy (Erdogan, 2000).

After that, Irwin with his colleagues found another important factor in the fracture of ductile materials: the plasticity. By adding both stored elastic energy and dissipated energy, which includes plastic dissipation and surface energy, the Griffith's energy equation was modified as follows (Irwin, 1957):

$$\sigma_f \sqrt{a} = \sqrt{\frac{EG}{\pi}} \tag{2.35}$$

where $G = 2\gamma + G_p$, $G$ is the total energy and $G_p$ is the surface energy due to the plastic deformation in ductile materials. From (2.35), the critical stress intensity factor was introduced by Irwin, which is in the form of

$$K_C = \sigma_f \sqrt{\pi a} \tag{2.36}$$

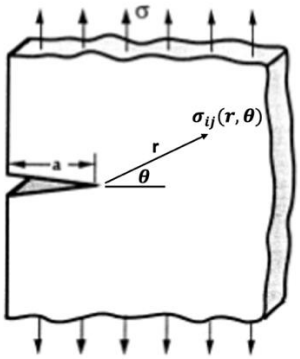


**Figure 6: Stress concentration near a crack tip**

Besides this, Irwin also found a way to calculate the stress field at the tip of a pre-existing crack, which can be written as (Freund, 1998):

$$\sigma_{ij}(r,\theta) = \left(\frac{K_I}{\sqrt{2\pi r}}\right) f'_{ij}(\theta) + \left(\frac{K_{II}}{\sqrt{2\pi r}}\right) f''_{ij}(\theta) + \left(\frac{K_{III}}{\sqrt{2\pi r}}\right) f'''_{ij}(\theta) \quad (2.37)$$

where $\sigma_{ij}$ is the stress tensor at the radial distance r from the crack tip with an angle of $\theta$ along the crack axis as shown in Figure 6. $f'_{ij}(\theta)$, $f''_{ij}(\theta)$, and $f'''_{ij}(\theta)$ are the dimensionless groups. $K_I$, $K_{II}$, and $K_{III}$ are the stress intensity factors corresponding to the three modes of fracture. For Mode I, $K_I$ is always designated as $K_{IC}$, which is the fracture toughness of the material. During the SAWs propagation, the stress at the crack tip will increase. Consequently, K will also increase. Once $K_I$ reaches $K_{IC}$ , the crack will start to open and propagate. Compared with the data measured from human kidney stones (Zhong et al., 1993), the borosilicate glass has a much higher fracture toughness as shown in Table 2. Now, if we substitute the fracture toughness value of borosilicate glass into Eqn. (2.36), the critical tensile stress required to initiate the fracture from the cracks introduced by microindentations, which have an average length of 100 μm, can be calculated as follows:

$$\sigma_f = \frac{K_{IC}}{\sqrt{\pi a}} = \frac{0.77\ MPa \cdot m^{\frac{1}{2}}}{\sqrt{\pi \cdot 100\ \mu m}} = 43.44\ MPa \quad (2.38)$$

**Table 2: Fracture toughness of renal calculi and borosilicate glass**

| Material | Fracture toughness, $K_{IC}$ (MPa $m^{1/2}$) |
|---|---|
| COM (100) | 0.136±0.021 |
| Brushite (95)/COM (5) | 0.119±0.030 |
| Uric Acid (100) | 0.090±0.028 |
| Borosilicate Glass | 0.770[1] |

However, it was suggested that the threshold based on the tensile stress only is not enough to predict the occurrence of ring-like fractures on the borosilicate glass under impact loading conditions (Zhang, 2018). Therefore, based on literature review, we have identified a dynamic failure criterion, which takes both magnitude and duration of the tensile stress pulse into consideration, to establish the threshold for crack extension on the glass surface caused by tensile stress pulses.

For a rectangular pulse to achieve fracture, the dynamic fracture criterion can be written as (Steverding and Lehnigk, 1976):

$$\frac{\sigma^2 \tau}{E} \geq \frac{\pi \gamma}{c} \tag{2.39}$$

[1] The data is retrieved from MatWeb.com.

where $\sigma$ is the pulse stress; $\tau$ is the pulse duration; E is the Young's modulus of the solids; $\gamma$ is the surface energy density for elastic deformation only; c is the sound wave speed in solids.

According to the pulse stress produced by NPL and the dominant role of LRWs in crack extension on the glass surface, Eqn. (2.39) can be rewritten in a general form as

$$\int_0^T \sigma_T^2 dt \geq \frac{\pi\gamma E}{c_{LRW}} \tag{2.40}$$

where $\gamma$ is 4.63 $Pa \cdot m$ ($or \frac{J}{m^2}$), E is 64 GPa, and $c_{LRW}$ is 3163 m/s for borosilicate glass. Then the critical threshold to initiate fracture obtained from the right-hand side of Eqn. (2.40) is 2.94 x $10^{-4}$ MPa · s. This value has the same order of magnitude with the threshold value of stress integral (SI) calculated by the Tuler-Butcher criterion, which is 2.4 x $10^{-4}$ MPa · s at a standoff distance of 3.0 mm (Zhang, 2018). It was observed experimentally that ring-like fracture could only be produced during NPL within a region of the borosilicate glass surfaces where the calculated SI value exceeding this damage threshold (Zhang et al., 2019).

## *2.4 Fractures induced by Vickers indenter*

The Vickers hardness test, also referred to as a microhardness testing, is a common method to characterize the hardness of various materials including metals, ceramics and etc. A square-based pyramid diamond indenter, which has an apex angle

of $136^0$, is pressed against the flat surface of the material with a certain load and a loading time of 10 to 15 seconds.

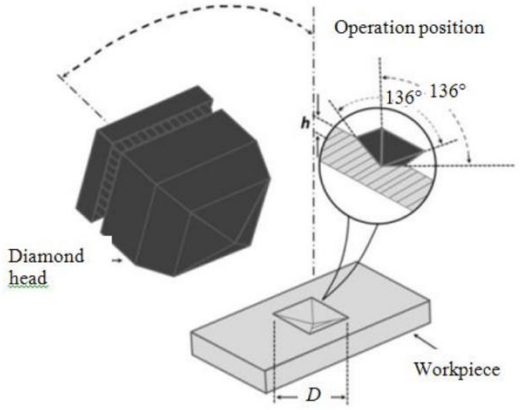


**Figure 7: Diamond indenter employed in the Vickers hardness test and its resulting indentation. D is the diagonal length of the indentation (Kah et al., 2013)**

By using the average of the two diagonals of the indentation (D) and the applied load F, the Vickers hardness (HV) of the material can be calculated by

$$HV = 0.1891\frac{F}{D^2} \tag{2.41}$$

and the indent depth (t) can be obtained according to the formula:

$$t = \frac{D}{2\sqrt{2}\tan\left(136°/2\right)} \tag{2.42}$$

In the last few decades, the indentation methods were also developed into an approach to determine the fracture toughness of the material based on the crack system developing from the indentation site during the contact loading and unloading on brittle solids. Figure 8 shows a common crack system produced by the Vickers hardness tester.

The Palmqvist cracks, which propagate from the vertices of the indentation site and remain close to the specimen surface are the first cracks to form during loading (Niihara, 1983). The median vent, which was first introduced by Lawn and Wilshaw in 1975, develops stably underneath the deformation-induced flaw under the increase in load and closes on unloading (Lawn & Wilshaw, 1975). The median cracks have a shape of penny and lies on a plane of symmetry containing the contact axis. Upon the complete unloading, the radial cracks driven by the residual stress have a significant growth and tends to have a half-penny geometry (Lawn, Evans, & Marshall, 1980). By measuring the final lengths of radials cracks, the fracture toughness ($K_{IC}$) of brittle materials can be obtained by the following equation (Anstis et al., 1981):

$$K_{IC} = 0.016 \left(\frac{E}{H}\right)^{\frac{1}{2}} \left(\frac{P}{c^{\frac{3}{2}}}\right) \tag{2.43}$$

where E is the Young's modulus, H is the Vickers hardness of the material, P is the indentation load, and c is the length of radial cracks.

After unloading, the lateral cracks will probably form underneath the plastic impression and propagate in a circular form on a plane parallel to the specimen surface. The dominant role of the residual stress was also identified during the lateral cracking (Lawn, Evans, & Marshall, 1982). Besides those primary cracks developing from the

indentation site, the other two types of cracks produced by Vickers indenter include secondary Palmqvist cracks and shallow lateral cracks.

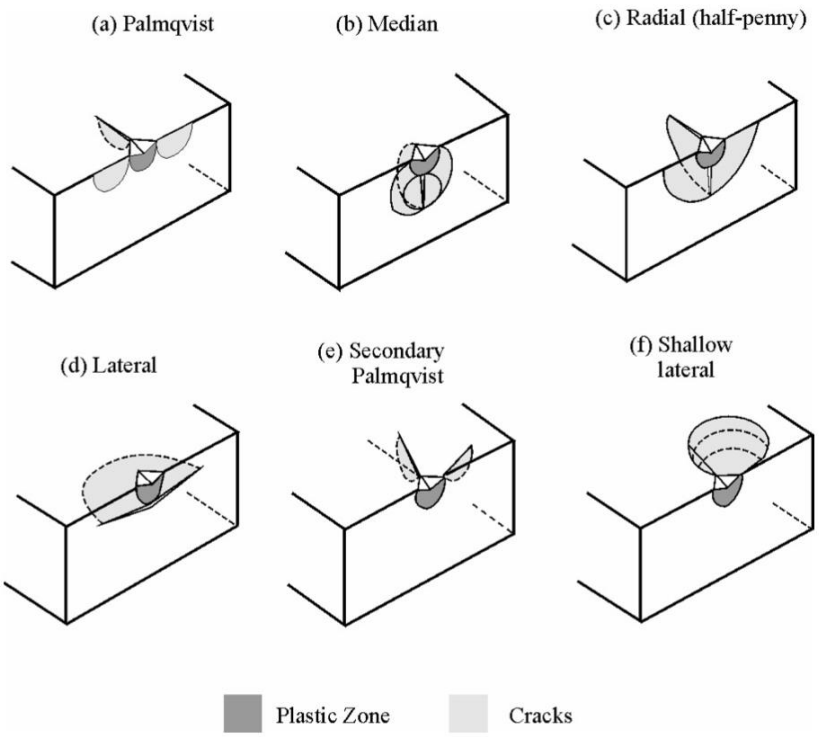


**Figure 8: The crack system created by a Vickers hardness tester (Szutkowska)**

# 3. Materials and methods

## *3.1 Experimental setup*

Figure 9 shows the experimental setup. A 3.6 Fr (1.2 mm in diameter) Nano Pulse Lithotripsy (NPL) probe (Lithotech Medical, Israel) operated at 10 kV was placed in front of a glass sample (50x50x3.3mm in LxWxH BOROFLOAT® Borosilicate Windows, Edmund Optics Inc.) to produce a shock wave via spark discharge. A 3D translational stage was used to adjust the standoff distance ($S_d$) between the glass sample and spark source. To capture the status of ring-like fracture formation after each shock, a high-speed camera (Phantom v7.3, Vision Research) was placed on the back side of the glass with a flat LED panel as a background.

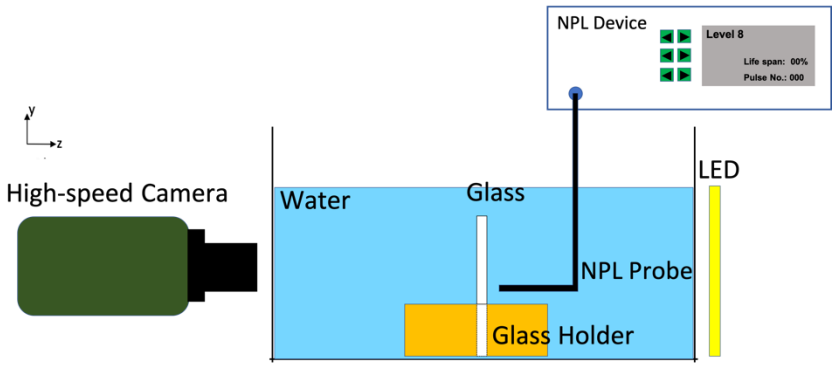


**Figure 9: A schematic diagram of the experimental setup**

In this study, a total of 28 glass samples were used, in which 12 measurements were first conducted using glass samples without indentations. The rest of the measurements were conducted on glass samples with indentations. On each sample

surface, four microindentations, created by a microhardness tester (HV-1000, AICEYI) using a Vickers indenter with a load of 1.0 kg and a dwell time of 10s, were placed around the center of the glass to minimize the effect of wave reflections from the glass boundaries. Each indentation site has an average diagonal length of 55 μm and the penetration depth of 7.8 μm, which is relatively shallow compared to the thickness of glass samples (i.e., 3.3 mm). The distances (R) between indentations and the center of glass (which is also referred as to the focal point, i.e., the projected center of the NPL probe on the glass surface) varies from 1.0 mm to 2.5 mm. Figure 10 demonstrates two typical settings of indentation locations. In each setting, two sets of axisymmetric indentations were placed along the x- and y-axis with the focal point at the center. In each measurement, the NPL treatment was terminated when the glass was broken.

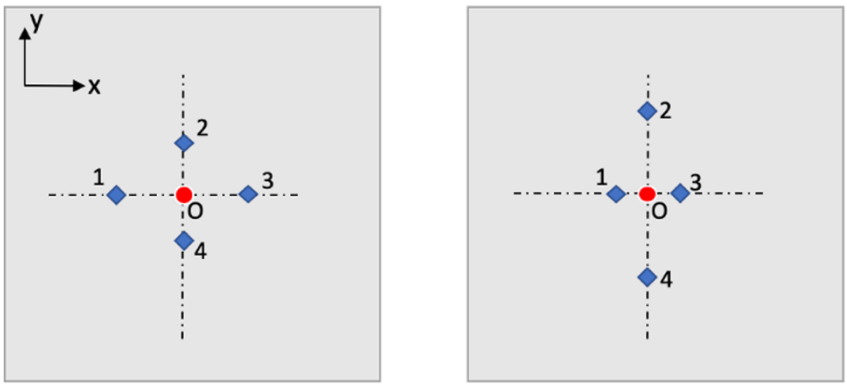


**Figure 10: Two typical settings of indentation locations with respect to the NPL probe projected focal point on the glass surface**

## *3.2 Optimal life span of the NPL probe*

To investigate the consistency of pulse energy generated by the NPL probe, a fiber optic probe hydrophone (FOPH-500, RP acoustics) was used to measure the pressure of the shock wave at three different radial distances along 30° (which is close to the critical incident angle for the excitation of a LRW at borosilicate glass-water boundary) from the probe axis as shown in Figure 11. At each radial distance, pressure waveforms of the first 100 shocks generated from a new NPL probe were collected by using a digital oscilloscope (HDO6104, Teledyne LeCroy Inc.).

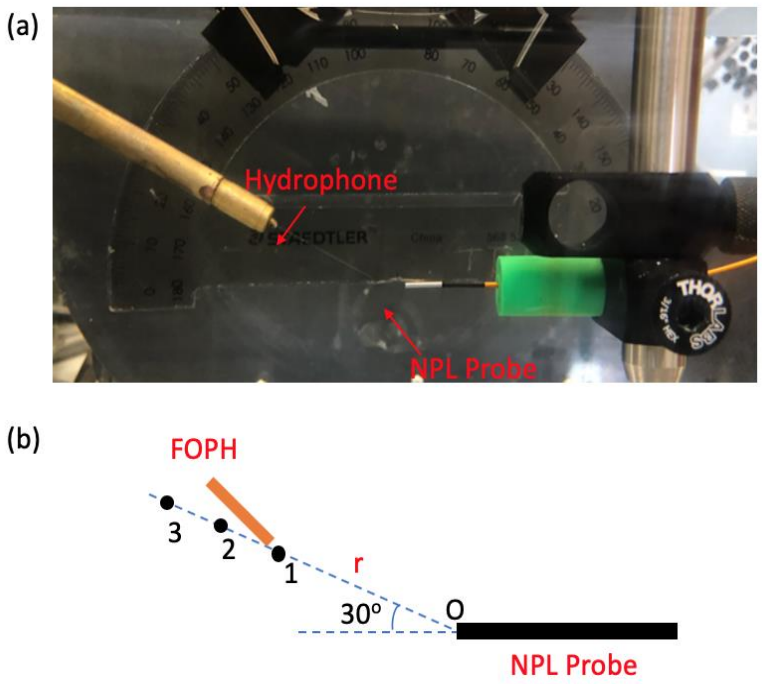


**Figure 11: (a) Experimental setup of measuring the pressure waveforms of NPL pulse energy by a fiber optic probe hydrophone (FOPH); (b) A Schematic diagram illustrating the hydrophone positions ($r_1$ = 7.10 mm, $r_2$ = 10.15 mm, and $r_3$ = 13.17 mm) and orientation (along 30° from the probe axis)**

Figure 12(a) shows the average pressure waveforms based on each 100 individual measurements at three radial distances ($r_1$ = 7.10 mm, $r_2$ = 10.15 mm, and $r_3$ = 13.17 mm). For each waveform, the leading shock front has a rise time of about 50 ns to reach to the peak pressure (p+), followed by a progressive decay in about 300 ns. As shown in Figure 12(b), p+ decreases inversely with the radial distance from the focal point, which is characteristic of a point shock wave source (Kinsler et al., 1999).

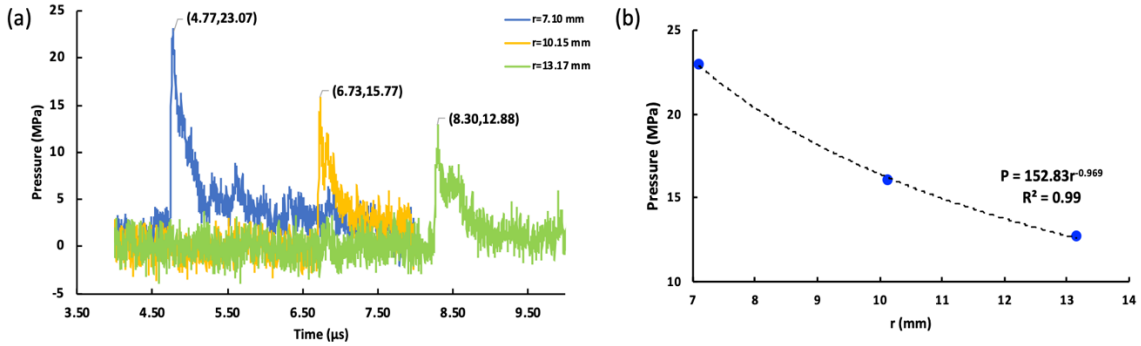


**Figure 12: (a) Averaged pressure waveforms of each 100 shocks generated by NPL probe at three radial distances (7.10 mm, 10.15 mm, 13.17 mm); (b) The relationship between peak value and radial distances**

Next, we compared the peak pressure variations within every 100 shocks to determine the optimal lifespan range of the NPL probe in the glass fracture experiment. As shown in Figure 13, we divided the 100 shocks into four regions based on the lifespan of the probe (displayed on the control panel of the NPL device) , including warm-up region (10 shocks), 98% - 91% of lifespan (40 shocks), 91% - 86% of lifespan (30 shocks), and 86% - 83% of lifespan (20 shocks). The peak pressure tends to increase overall in the warm-up region before reaching a fluctuating stage. At $r_1 = 10.15$ mm, the average p+ value of the whole range except the warm-up region is 16.06 MPa with a coefficient of variance (CV) of 13.76%. The 98% - 91% region has the highest average peak pressure with the largest standard deviation.

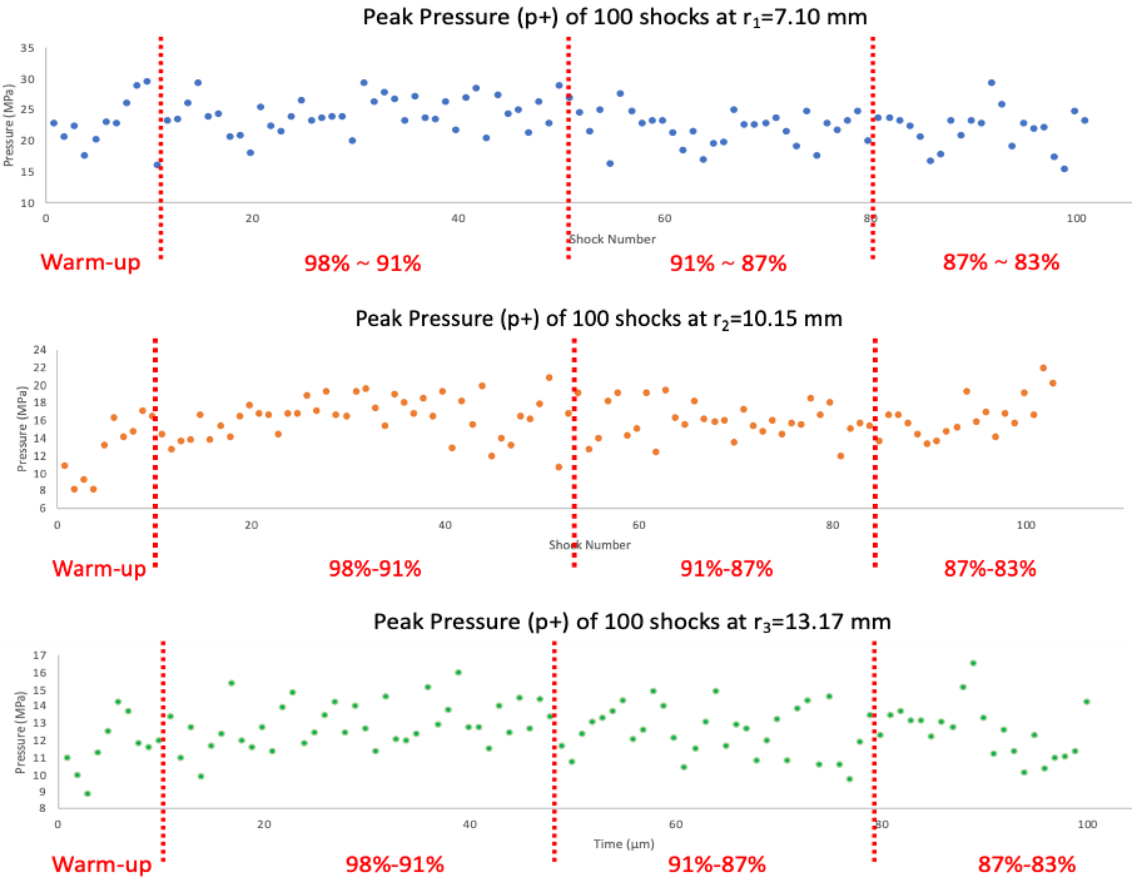


**Figure 13: Peak pressures of 100 shocks at $r_2$ = 10.15 mm**

The situation is very similar in the other two conditions ($r_1$ = 7.1 mm and $r_3$ = 13.17 mm). At 7.1mm radial distance, the average peak pressure slightly decreases as the probe lifespan goes downward. In the range of 91% - 87% and 87% - 83% lifespan, the pulse energy is relatively consistent.

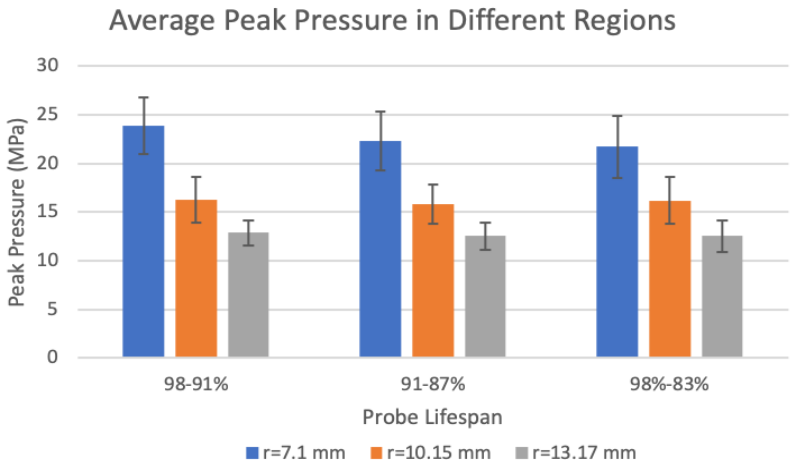


**Figure 14: Statistical analysis of the average peak pressure among three lifespan regions at various radial distances**

Besides the variants of pulse energy for each probe, the pulse duration is another import factor in the performance of NPL treatment. At the radial distance of 7.1 mm, we extracted five pressure waveforms from each region and compared their averaged values as shown in Figure 15. We found that in 98% - 91% life span region, the rise time of the leading shock front is the shortest one. As the probe lifespan decreases to 87% - 83%, more time is needed for the pressure to reach its peak value, followed by a longer progressive decay.

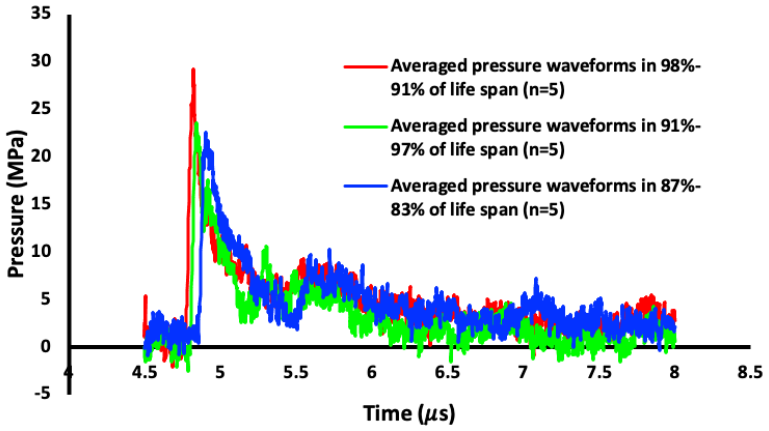


**Figure 15: Pressure waveforms in different regions of NPL probe lifespan**

These pressure measurement results are consistent with the preliminary fracture test results on the glass, i.e., the probe with higher lifespan (98% - 91%) has high possibility to break glasses in 6-10 shocks, while in the lower lifespan (91% - 83%), 16-20 shocks are needed to fracture the glass. Since more shock waves will be favorable to observe the overall processes of ring-like fracture and crack extension from pre-existing or artificially induced surface flaws, we finally determined to use the probe with 91%-83% lifespan to conduct the experiments.

## *3.3 Selection of standoff distance and indentation position*

Previous study has shown that the nanosecond shock waves produced by NPL probe can create ring-like fracture patterns on the glass surface (Zhang et al., 2019). The radius of the ring fracture varies significantly even at a fixed standoff distance ($S_d$)

between the NPL probe and the glass surface. At $S_d$ = 0.5 mm, the ring radius varied approximately from 0.25 mm to 1.75 mm, compared 0.6 - 2 mm at $S_d$ = 1.0 mm (Zhang et al., 2019). As $S_d$ increases, the range of the radius for the ring fracture decreases. In this study, the standoff distance was fixed as 1.5 mm, which has a relatively narrow range of ring radius (1.25-2.25 mm). In the previous study (Zhang et al., 2019), the shock number required to form a ring fracture was about 29. However, in our experiments, a much lower shock number (<18) was observed before the glass breakage. This discrepancy may be caused by the different probe lifespan ranges used in the two experiments.

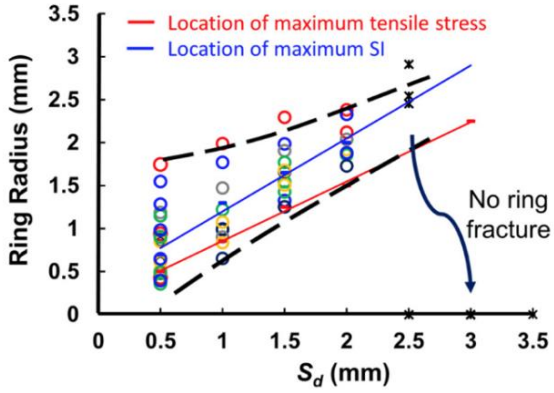


**Figure 16: The radius of ring-like fracture produced on the glass surface (Zhang et al., 2019)**

To determine the locations of micro-indentations, we investigated the first principal stress ($\sigma_{T,max}$) produced along the water-glass boundary and the stress integral (SI) obtained in the previous numerical modeling (Zhang et al., 2019). When $S_d$ was 1.5 mm, $\sigma_{T,max}$ increased rapidly to a peak value when the radial distance was between 0 -

1.2 mm. Then $\sigma_{T,max}$ decreased gradually until reaching the boundary. Based on the Tuler-Butcher criterion, the stress integral (SI) threshold ($2.4 \times 10^{-4} MPa \cdot s$ at $S_d$ = 3.0 mm) was used to predict the NPL-produced damage on glass surface. As shown in Figure 17, the SI values of $S_d$ = 1.5 mm curve were higher than the threshold value when the radial distance is in the range of 1.2 mm – 2.3 mm. Therefore, we finally chose 4 feasible radial distances to locate microindentations (1.0 mm, 1.5 mm, 2.0 mm and 2.5 mm) to investigate the effect of artificial surface flaws on the damage threshold.

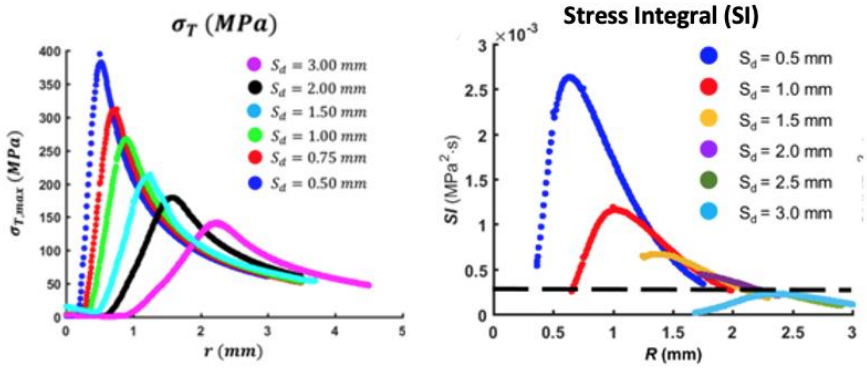


**Figure 17: The radial distribution of $\sigma_{T,max}$ (left) and SI (right) at various $S_d$ (Zhang et al., 2019)**

## *3.4 Artificial surface flaws created by the Vickers indenter*

In order to simulate the surface flaws induced by cavitation in SWL, the micro-indentation produced by the Vickers indenter was applied on the glass surface. Figure 14(a) shows a typical indentation created by a load of 0.2 kg and a dwell time of 10 s on the glass surface. The indentation has a shape of diamond with no cracks extending

from the four vertices. By contrast, a microindentation produced by a load of 1.0 kg and the same dwell time is shown in Figure 18(b). Five specific characteristics of this indentation are labelled in Figure 18(c). The first characteristic is the central plastic deformation (PD) region with diamond-shape, which has an average diagonal length of 55 μm. Second, four primary radial cracks (RC) propagates from the vertices of diamond with a length of 20 μm. Third, six secondary Palmqvist cracks (SP) extends from the center of indentations, whose lengths are in the range of 37-70 μm and the typical width of the crack lines is about 1 - 2 μm. Compared with the indentation created by smaller load, the third characteristic is the damage under the central diamond, which is referred as to the shallow lateral cracks (SL). Finally, the "external circle" pattern with a radius of 86 μm is presumably caused by the residual stress, which has the same feature with lateral cracks (LC) mentioned in Figure 8(d).

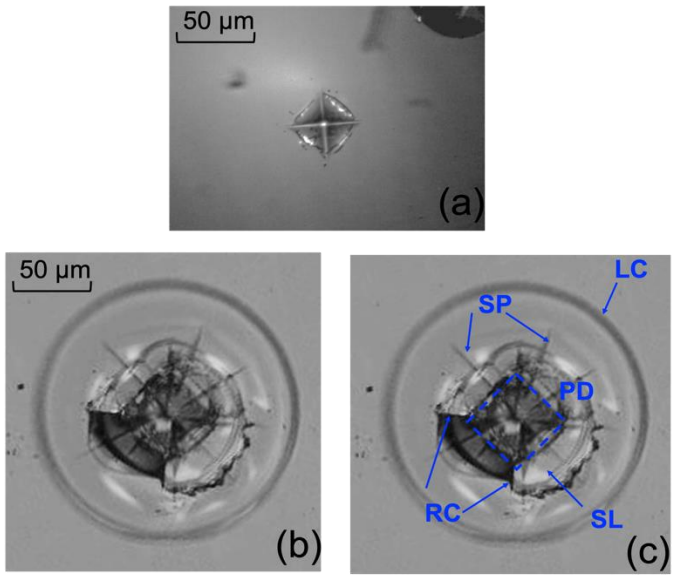


**Figure 18: (a) An indentation created by a load of 0.2 kg and a dwell time of 10 s; (b) An indentation created by a load of 1.0 kg and a dwell time of 10 s, and (c) Five characteristics of indentation**

# 4. Crack development from microindentations

## *4.1 Cracks along two different orientations*

Figure 19 illustrates the location and orientation of each indentation created on the glass surface. Point O represented the projected center of NPL probe on the glass surface, which is also regarded as the focal point. The indentations were placed at different radial distances (R = 1.0, 1.5, 2.0, 2.5 mm) from point O and the orientation of each indentation was based on its two diagonals. One diagonal was kept paralleled to the direction of SAWs propagation ($D_{0\ deg}$) and the other was spontaneously perpendicular to the SAW direction ($D_{90\ deg}$). For each microindentation, we compared the crack development in these two directions ($D_{0\ deg}$ and $D_{90\ deg}$) to assess the effect of stress field produced by SAWs.

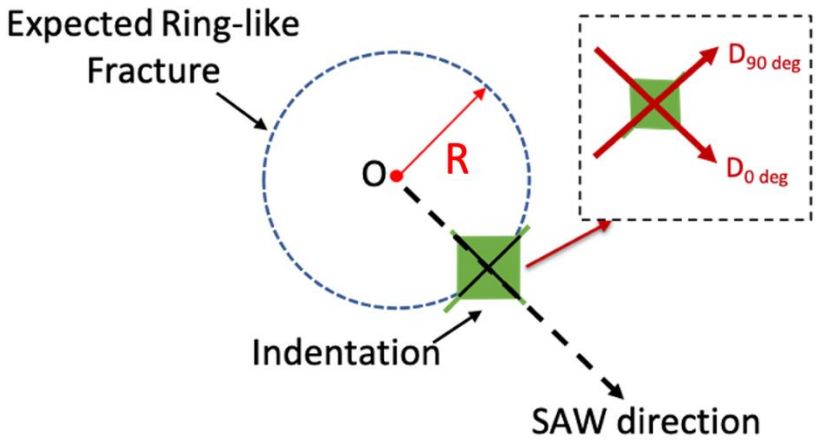


**Figure 19: A schematic diagram of indentation location and orientation**

Table 3 presents four typical indentations at different radial locations, which were recorded under 10x microscope. The appearance of indentation impressions and initial crack lines formed in various directions before NPL treatment is listed in the first row and the second row shows the crack development from each indentation after 10, 6, 8 and 8 shocks, respectively. The direction of the SAW propagation is indicated by the blue arrows. The first noticeable difference between the two rows is the size and appearance of indentation impression before and after the shock wave treatment. The damage area around the central part of the indentation appeared to be broadened. At the R = 1.5 mm indentation, the damage even propagated to the original "external circle", which is presumably caused by the residual stress after unloading. This observation indicates that the interaction NPL-generated SAWs with the indentation impression can produce strong tensile or shear stresses that extend the crack lines produced by the microindentation. Second, in particular, the radial cracks extended along the indentation diagonal in the $D_{90\ deg}$ direction, which are pointed out by yellow arrows, were much longer than in the $D_{0\ deg}$ direction. The results of previous model simulations in NPL have demonstrated clearly that the glass surface during SAW propagation is under biaxial tension with the tensile stress component along the radial direction significantly greater than along the circumferential direction (Zhang et al., 2019). For the R = 1.0 mm indentation, a small crack, marked by a red arrow in Table 3,

developed horizontally towards the focal point; at 1.5 mm, no cracks developed along $D_{0\ deg}$; in the other two cases, the cracks starting from the external circle propagated northeast presumably due to the asymmetric damage around the indentations. Therefore, it can be concluded that SAWs induced tensile stress were primarily responsible for the extension of crack lines and their subsequent development, despite the fact that there were multiple crack lines emanated from the indentation site in different orientations. Third, among these four cases, the cracks developing circumferentially along the $D_{90\ deg}$ direction were not perfectly smooth and continuous. This phenomenon implies that these crack segments might be extended by different shock pulses.

**Table 3: Images of four typical microindentations at different radial distances from the focal point before and after NPL treatment. The blue arrow indicates the propagation direction of the LRW produced by NPL.**

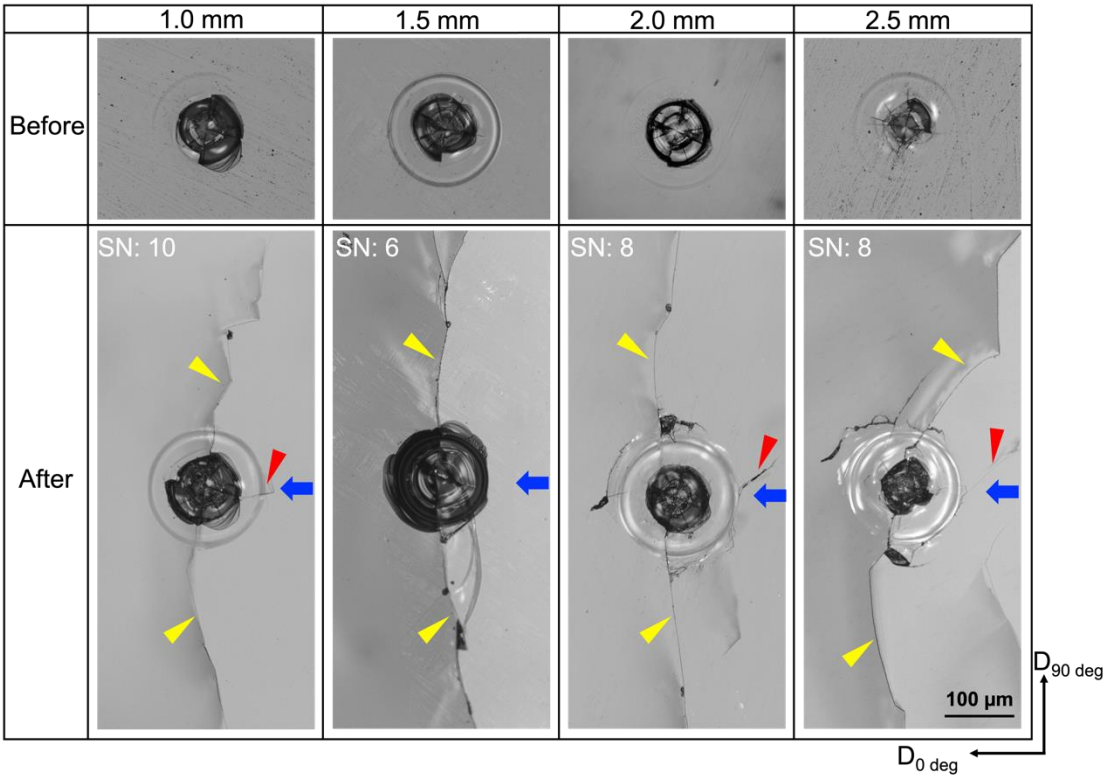


## *4.2 Crack formation from microindentations at various locations*

In a previous COMSOL model, the distribution of maximum tensile stress ($\sigma_{T,max}$) and stress integral (SI) at the water-glass boundary were calculated at various standoff distances (Zhang, 2018), which have been shown in Figure 17. At $S_d$ = 1.5 mm, the calculated $\sigma_{T,max}$ first increased to the peak value at the approximate radial distance of 1.2 mm then decreased gradually; the peak value of SI occurred around the radius of 1.5

mm then declined until reaching the simulation boundary. Therefore, we anticipated that if the microindentation-induced surface flaws are placed at various locations on the glass surface, the speeds of crack extension will vary.

We recorded the appearance of indentations after each shock and the details of crack extension are presented in Table 4. When the indentation was placed at R = 1.0 mm, the crack lines first appeared after 1 shock then extended both upward and downward along the $D_{90\ deg}$ direction simultaneously under the treatment of subsequent shock pulses. At the R = 1.5 mm indentation, no visible crack extensions were observed after the first three shocks. Starting from the fourth shock, the crack lengthened progressively until the glass was broken at SN = 8. At the R = 2.0 mm indentation, some surface flaws formed on the top of indentation at first then the cracks grew rapidly after $5^{th}$ shock. At the R = 2.5 mm indentation, the first appearance of the crack was postponed after $7^{th}$ shock. In conclusion, as the distance between the microindentation and focal point becomes larger, more shocks are required to initiate crack extension from the indentation site. This phenomenon can be first explained by the theory that the stress concentration caused by indentations at the crack tip can greatly reduce the required tensile stress to initiate a crack extension (Lawn, 1993). Then, based on the radial distribution of $\sigma_{T,max}$ and SI, it can be further concluded that when the microindentation

is closer to the radial distances at which the peak value of $\sigma_{T,max}$ and SI reached, fewer shocks will be needed to initiate the crack extension from it.

**Table 4: Crack extension from four indentations at different radial distances from the focal point. The images were recorded after each shock by Phantom camera.**

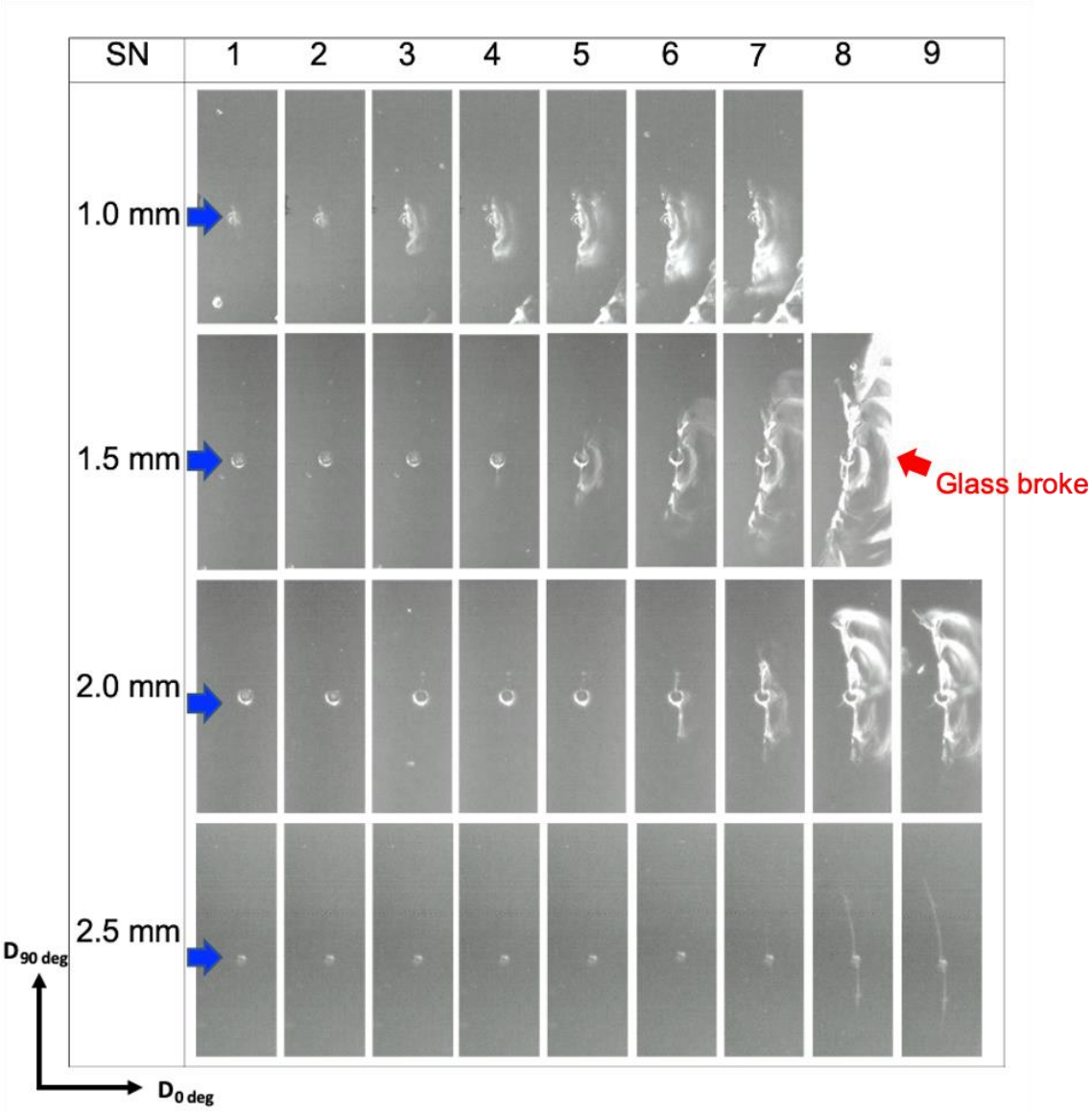

## 4.3 Statistical analysis and discussion

To investigate the effect of SAWs on the speed of crack extension, we recorded the central angle of cracks after each shock then calculated the approximate arc length by multiplying the central angle (in radians) with the radius. The sample size at each indentation radius is 5. As shown in Figure 21, the starting point of each curve represents the shock number required to initiate the extension of the observable crack. Among four curves, the cracks developing from the 1.5 mm indentations were the longest ones. For example, at SN = 5, the arc lengths of 1.0, 1.5, and 2.0 mm indentation were 0.82 mm, 1.44 mm, and 0.53 mm, respectively; at SN = 8, the cracks from 1.5, 2.0 and 2.5 mm extended to 2.59 mm, 1.42 mm, and 0.39 mm, respectively.

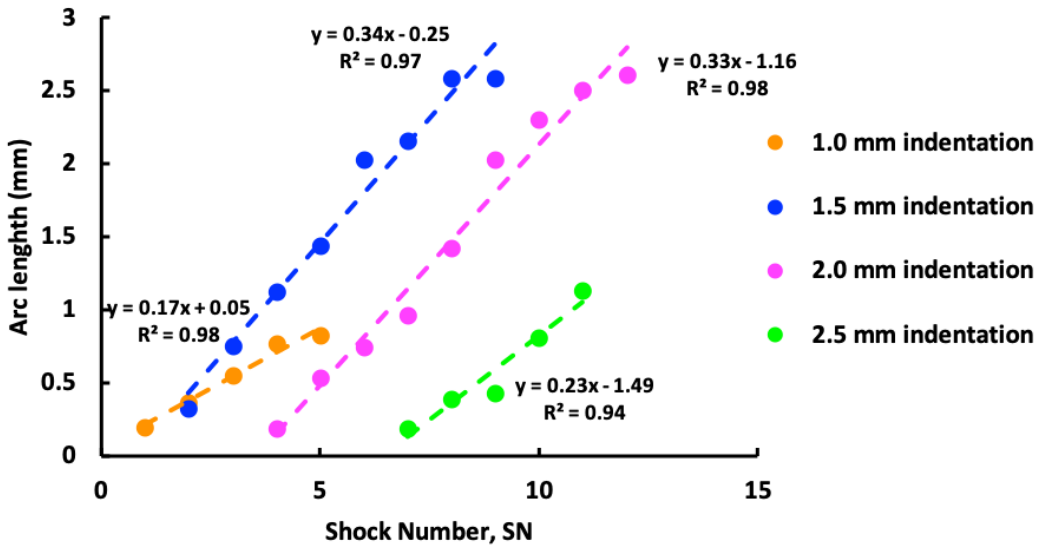


**Figure 20: Crack formation process from four various microindentations. Each point represents the average value of five data sets.**

For each indentation, there is an approximately linear relationship between shock waves delivered and the accumulated crack lengths, i.e., as the shock number increased, the crack lengths became larger. At the 1.0 mm indentation, the crack extension was initiated after the 1st shock and its arc length was increased to 0.82 mm after the 5th shock.

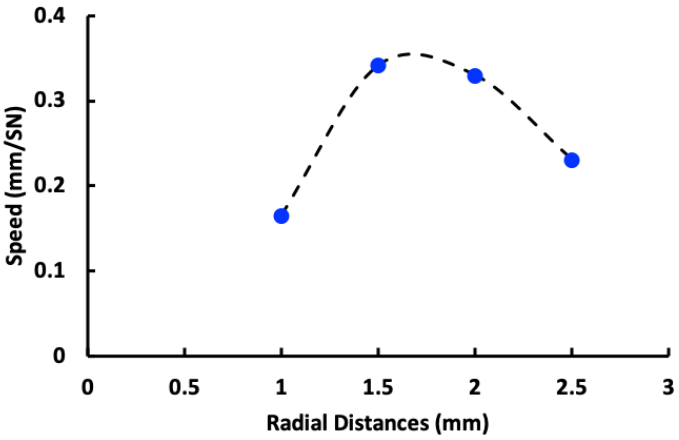


**Figure 21: The relationship between radial distances and crack development speed**

Based on the trendline added on each set of data, we can calculate the slope of each curve, which represents the average speed of crack extension in mm/SN (arc length/shock number). As shown in Figure 22, the speed of crack extension at the R = 1.0 mm indentation was the lowest one. Then the estimated speed increased gradually and reached the peak value between the R = 1.5 mm and the R = 2.0 mm radial distances, with a corresponding slope of 0.34 mm/SN and 0.33 mm/SN, respectively. Finally, the

speed drops to 0.23 mm/SN at the R = 2.5 mm indentation. Interestingly, the shape of this trendline is similar with the distribution of $\sigma_{T,max}$ and SI obtained by the mathematical simulation (Zhang et al., 2019), which implies that speed of crack development would be highly associated with the change of local tensile stress and SI on the glass-water boundary. In addition, we correlated the radial distance and speed of crack development by performing a regression analysis. Based on the t-tests, the P-value were calculated to be 0.0102, i.e., $P<0.05$, indicating a statistical significance between these two variables.

# 5. Ring fractures

## *5.1 Formation of ring fracture without microindentations*

In total, we did 12 measurements on the glass without microindentations and found that the radius of ring-like fracture was in the range of 1.33 - 2.26 mm. Before the glass broke, the longest ring fracture had a central angle of 188 degrees after 18 shocks. By contrast, the longest crack extending from microindentations was an arc with a central angle of 99 degrees after 9 shocks. Figure 23 shows a typical process of ring-like fracture formation on the glass surface. Since the probe would change its position after each shock, a black dot was marked in the middle of each sample to confirm the coincidence between focal point and the center of NPL probe. At the $4^{th}$ shock, some surface flaws appeared at the radial distance of 2.06 mm then developed into a small crack with the central angle of $14.35^{o}$ after the $5^{th}$ shock. During the subsequent 11 shocks, this small crack extended along a circular path and finally developed into an arc with a central degree of $168.32^{o}$. This fracture formation was driven by the local tensile stress field induced by SAWs (Ying et al, 2019), which is consistent with the first mode of fracture (Lawn, 1993). In addition, after the $6^{th}$ shock, a second ring fracture appeared with a radius of 1.2 mm, which did not develop further until the last shock. This second ring-like fracture always had smaller radius than the first one, indicating the possibility that the second ring-like fracture might be produced by the tensile stresses generated by the reflection of LRW from the first ring fracture.

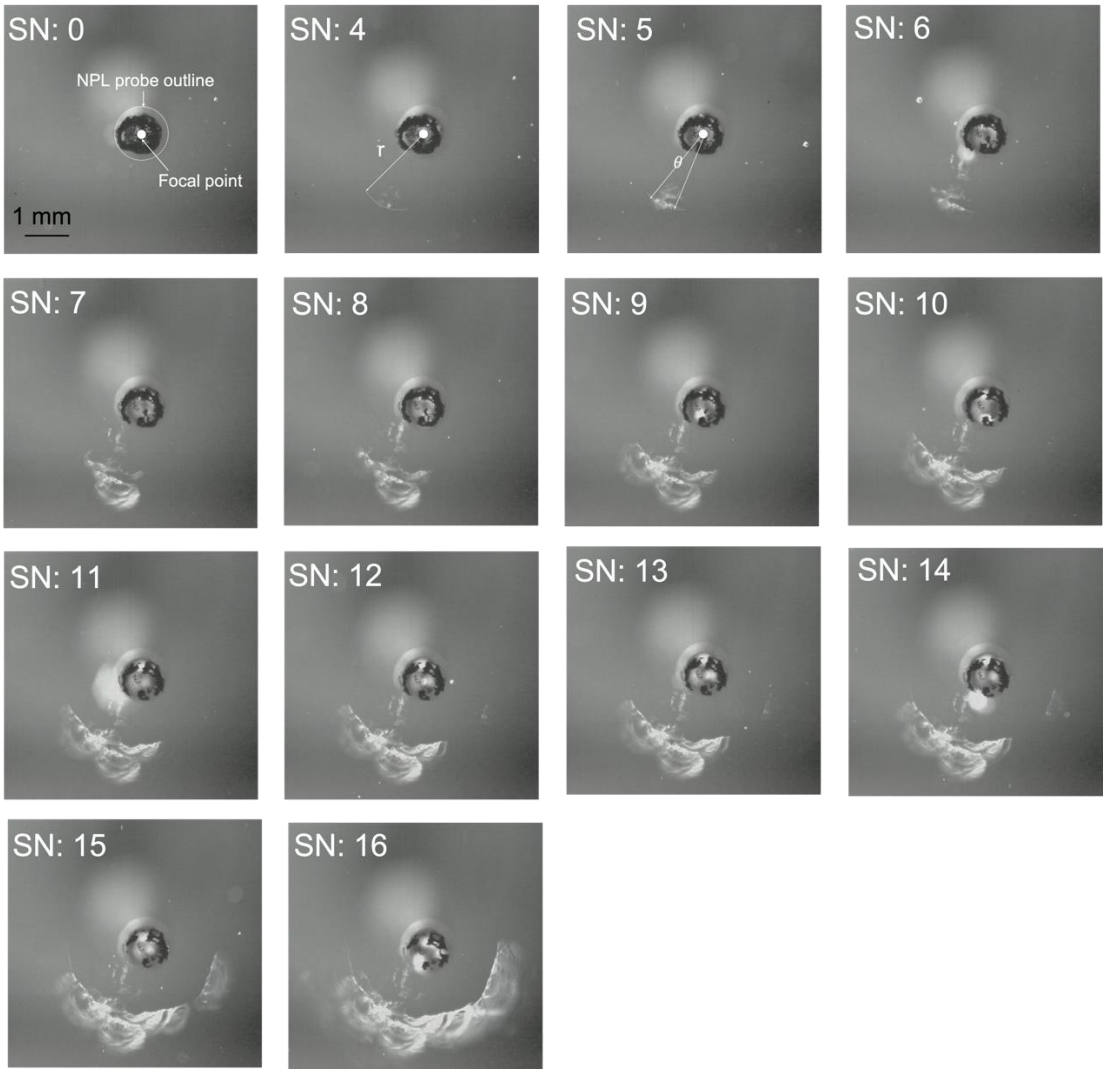


**Figure 22: The formation of ring-like fractures on the glass surface without microindentations.**

By collecting the data of arc lengths after each shock, the average formation process of the first appeared ring-like fracture, which had a radius in the range of 1.23 mm - 1.85 mm was plotted in Figure 24. The first visible ring fracture with an arc length

of 0.33 mm appeared after the 4th shock and thereafter the crack extended at an average speed of 0.228 mm/SN.

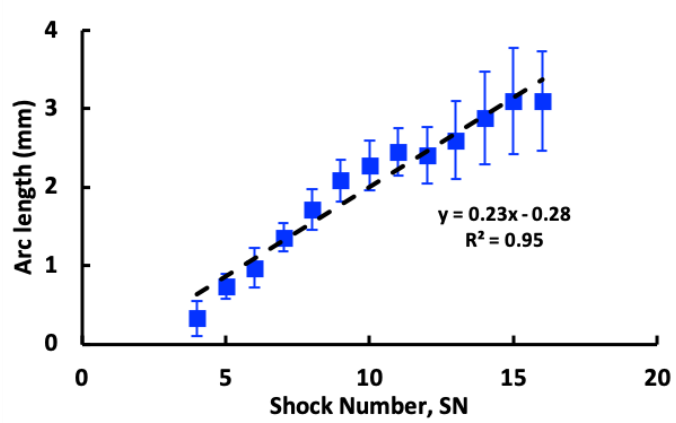


**Figure 23: The process of ring-like fracture formation on the glass without indentations with a linear fitting curve.**

## *5.2 Ring radius differences between the glass with and without indentations*

According to the previous study, the possible radius of ring fracture was in the range of 1.3 - 2.2 mm when the standoff distance is 1.5 mm (Zhang et al., 2019). This range would become narrow at larger standoff distances. In this study, two sets of indentation-created surface flaws on the glass surface were outside this range, but the crack lines still extended under the treatment of NPL shockwaves. The radii of the ring-like fracture after the final shock before glass failure (i.e., breaking into two pieces) were shown for both with and without indentations cases in Figure 25. Most glass samples with indentations could tolerate fewer shock pulses before its final failure, suggesting that the artificially-induced surface flaws could significantly weaken the strength of the

material surface. For the glass samples with indentations, the crack lines developed from the 1.0 mm indentations and 1.5 mm indentations were detected on the glass surface. In both cases, the crack lines all appeared in the region where no ring fracture were observed on the glass surfaces without indentations. Although the maximum tensile stress induced by SAWs was strong enough in a specific range to induce the fracture on the glass surface compared with the typical tensile strength of a glass sample (SCHOTT, 2007), both SI and the pulse duration have been proved to play an important role in the fracture initiation and subsequent propagation (Zhang et al., 2019). The existence of microindentation impressions and associated surface flaws produced would presumably weaken the material surface in tension as well as the surface energy density. Consequently, the nominal SI threshold for crack extension from the indentation sites will also be reduced based on Eqn. (2.40).

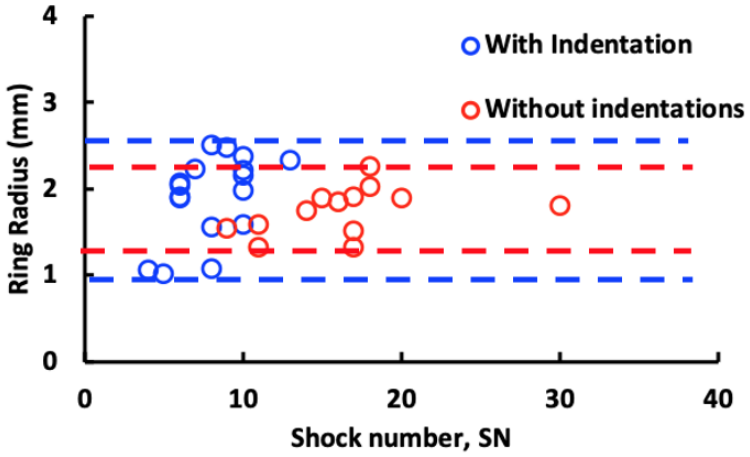


**Figure 24: The comparison of ring radius between the glass with and without indentations cases**

## *5.3 Speeds of crack extension*

In order to investigate the effect of indentation-induced surface flaws on the speed of ring-like fracture extension, we extracted and compared two sets of data from the previous results based on their ranges of ring radius. These are the data from the R = 1.5 mm indentations, and the average value of five glasses without indentation, which had ring-like fracture formation with the radii of 1.43, 1.59, 1.52, 1.54 and 1.46 mm, respectively. As shown in Figure 24, the first observable crack developed from the R = 1.5 mm indentations was after the second shock, while for the glass samples without indentations the first crack was produced after the $4^{th}$ shock. These findings suggest that the surface flaws produced by microindentations may provide surface crack lines sufficiently large to be extended by NPL-generated SAWs. Consequently, fewer shocks were required to drive the crack extensions from the R = 1.5 mm indentations. Moreover, the slope of the R = 1.5 mm indentation curve is relatively steeper than the ring-like fracture curve without indentations. This difference may indicate that less tensile stress energy is required to extend the opening of the crack line from the indentation-produced surface flaws within a specific range of radial distances.

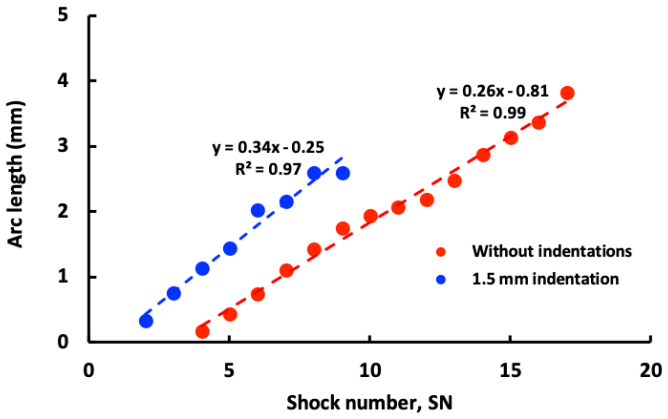


**Figure 25: Comparison of crack formation speeds between the glass without indentations and with indentations at the R = 1.5 mm from the focal point**

# 6. Conclusion

## *6.1 Summary of the thesis*

Cavitation is an important mechanism of stone fragmentation in SWL, in which it is difficult to separate the effects of cavitation from stress waves, including surface acoustic waves because they often happen simultaneously. However, in NPL, the effect of cavitation during the initiating of fracture lines is negligible and compared with SWL, the pulse energy derived by NPL under the fixed standoff distance can be easily controlled. Therefore, the primary goal of this thesis research is to investigate the individual effect of cavitation damage (mimicked by microindentation produced surface flaws) and stress fields induced by SAWs through conducting the experiments on the borosilicate glass under well-controlled conditions.

The details of experimental setup were presented in Chapter 3. Four microindentations at various radial distances were created on the glass surface by using a Vickers indenter with a load of 1.0 kg and a dwell time of 10 s. The choice of indentation size was mainly based on the surface erosion size caused by cavitation in SWL. The selection of NPL probe lifespan aimed to apply relatively stable pulse energies to individual glass samples. The indentation locations and standoff distance were determined by the maximum tensile stress along the glass-water boundary as reported in the previous study.

Chapter 4 is comprised of two parts. In the first part, the crack progression along two diagonals of the indentations were compared to investigate the effects of the stress fields generated by SAWs on crack extension. One diagonal was parallel to the SAWs propagation and the other direction was spontaneously perpendicular to the SAWs propagation. Based on the results, we concluded that the local maximum tensile stress played a dominate role in the crack extension from each indentation site and the increase of damage area around the indentation. In the second part, the expansion speed of the cracks initiated from indentation sites produced at different radial distances from the focal point was analyzed. Crack extension from the R = 1.5 mm indentations was found to have the fastest speed while the ones from the R = 1.0 mm indentations showed the lowest speed of crack propagation.

Next, we compared the speed of crack expansion from the R = 1.5 mm indentation sites with the speed of ring-like fracture formation at about the same radial distance on the glass surfaces without microindentations in Chapter 5. We found that the introduction of surface flaws by microindentations could lead to crack development in the region where no ring-like fracture were observed under the experimental conditions (i.e., same NPL probe, output energy and at the same standoff distance). Moreover, the artificial surface flaws induced by the microindentations were found to speed up the formation and expansion of surface fracture lines.

## 6.2 Recommendation for future work

In this study, we conducted the experiments by NPL probe to investigate the effect of stress fields induced by surface acoustic waves on the artificial surface flaws, such as those produced by cavitation damage in SWL. The reason why these pre-existing microindentations can speed up the formation of fractures on the glass surface needs further investigation. At the tip of indentation-induced surface flaws, the stress concentration may reduce the tensile stress or stress integral, and the number of shock waves required to drive the extension of the crack. To better understand the physical mechanism responsible for the experimental observations in this study, it will be valuable to construct a COMSOL model, in which the surface flaws with uniform size and surface flaws are embedded in the glass surface to investigate the change in the stress field on the glass-water boundary during NPL treatment. To test the numerical model validation, a dynamic brightfield photoelastic/shadowgraph imaging system (Xi & Zhong, 2001) can be applied to visualize the generation and propagation of SAWs at the water-glass boundary with microindentations applied on the glass surface.

Furthermore, due to the large size and thickness of the glass samples used in this study, leaky Raleigh waves dominated the crack extension and ring-like fracture formation in the experiments. To gain further insights into the fundamental mechanism of stone comminution by shock waves, future studies should be conducted under the treatment of NPL by reducing the size and thickness of glass samples to investigate the

effect of other types of SAWs, and their potential interaction with reflected bulk elastic waves and their impact on stone fracture.

# References


Anstis, G., Chantikul, P., Lawn, B., & Marshall, D. (1981). A Critical Evaluation of Indentation Techniques for Measuring Fracture Toughness: I, Direct Crack Measurements. *Journal of the American Ceramic Society*, 64(9), 533–538.

Bowden, Frank Philip, and John Edwin Field. (1964). The brittle fracture of solids by liquid impact, by solid impact, and by shock. *Proceedings of the Royal Society of London. Series A. Mathematical and Physical Sciences*, 282(1390), 331-352.

Buck O, Thompson RB, Rehbein DK. (1988). Using acoustic waves forthe characterization of closed fatigue cracks. In: Newman Jr. JC,Elber W, editors. *Mechanics of fatigue crack closure*, ASTM STP982, p. 536–47.

Brekhovskikh, L.M., Godin, O.A.: Acoustics of Layered Media I: Plane and Quasi-Plane Waves. *Springer Series on Wave Phenomena*. Springer (1990)

Cleveland, R. O., and Sapozhnikov, O. A. (2005). Modeling elastic wave propagation in kidney stones with application to shock wave lithotripsy. *The Journal of the Acoustical Society of America*, 118(4), 2667-2676.

Coleman, A. J., Saunders, J. E., Crum, L. A., & Dyson, M. (1987). Acoustic cavitation generated by an extracorporeal shockwave lithotripter. *Ultrasound in Medicine & Biology*, 13(2), 69–76.

Erdogan, E. (2000) Fracture Mechanics, *International Journal of Solids and Structures*, 37, pp. 171–183.

FRACTURE TOUGHNESS DETERMINATION OF COMPOSITES BASED ON ... (n.d.). Retrieved from http://www.escm.eu.org/docs/eccm/C185.pdf

Freund, L.B. (1998). Dynamic fracture mechanics, *Cambridge Monographs on Mechanics. Cambridge University Press*

Griffith, A.A. (1921). The phenomena of rupture and flow in solids. *Philosophical Transactions of the Royal Society of London Series a-Containing Papers of a Mathematical or Physical Character* 221, 163–198.

Gusev, V., Desmet, C., Lauriks, W., Glorieux, C., and Thoen, J. (1996). Theory of Scholte, leaky Rayleigh, and lateral wave excitation via the laser-induced thermoelastic effect. *J. Acoust*. Soc. Am. 100, 1514–1528.

Irwin, G. (1957). Analysis of stresses and strains near the end of a crack traversing a plate, *Journal of Applied Mechanics* 24, 361–364.

Kah, P., Olabode, M., Hiltunen, E., & Martikainen, J. (2013). Welding Of A 7025 Al-Alloy By A Pulsed Mig Welding Process. *Mechanika,* 19(1).

Kaplan, A. G., Chen, T. T., Sankin, G., Yang, C., Dale, J. A., Simmons, W. N., … Lipkin, M. E. (2016). Comparison of the Nanopulse Lithotripter to the Holmium Laser: Stone Fragmentation Efficiency and Impact on Flexible Ureteroscope Deflection and Flow. *Journal of Endourology*, 30(11), 1150–1154.

Khuri-Yakub, B.T., Kino, G.S., Evans, A.G., 1980. Acoustic surface wave measurements of surface cracks in ceramics. *J. Am. Ceram.Soc*. 63 (1,2), 65–71

Kinsler, L. E., Frey, A. R., Coppens, A. B., & Sanders, J. V. (1999). Fundamentals of acoustics. Fundamentals of Acoustics, 4th Edition, by Lawrence E. Kinsler, Austin R. Frey, Alan B. Coppens, James V. Sanders, pp. 560. ISBN 0-471-84789-5. Wiley-VCH, December 1999., 560.

Lawn, B., & Wilshaw, R. (1975). Indentation fracture: principles and applications. *Journal of Materials Science*, 10(6), 1049–1081.

Lawn, B. R., Evans, A. G., & Marshall, D. B. (1980). Elastic/Plastic Indentation Damage in Ceramics: The Median/Radial Crack System. *Journal of the American Ceramic Society*, *63*(9-10), 574–581.

Lawn, B. (1993). Fracture of Brittle Solids. *Cambridge: Cambridge University Press.*

Lomonosov, A. M., and Hess, P. (2002). Impulsive fracture of silicon by elastic surface pulses with shocks. *Physical review letters* 89(9).

Marshall, D., Lawn, B., & Evans, A. (1982). Elastic/Plastic Indentation Damage in Ceramics: The Lateral Crack System. *Journal of the American Ceramic Society*, 65(11), 561–566.

Mendelsohn, D.A., Achenbach, J.D., Keer, L.M.(1980). Scattering of elastic waves by a surface-breaking crack. *Wave Motion* 2, 277–292.

Niihara, K. (1983). A fracture mechanics analysis of indentation-induced Palmqvist crack in ceramics. *Journal of Materials Science Letters*, 2(5), 221–223.

Nkemzi, D. (1997). A new formula for the velocity of Rayleigh waves. *Wave Motion 26*, 199-205.

Pishchalnikov, Y. A., Sapozhnikov, O. A., Bailey, M. R., Williams, J. C., Cleveland, R. O., Colonius, T., … Mcateer, J. A. (2003). Cavitation Bubble Cluster Activity in the Breakage of Kidney Stones by Lithotripter Shockwaves. *Journal of Endourology*, 17(7), 435–446.

Rayleigh, J.W.S. (1887). On waves propagating along the plane surface of an elastic solid. *Proc. London Math. Soc. 17*, 4-1.

SCHOTT. (2007). SCHOTT Technical Glasses Physical and technical properties. *Germany: SCHOTT.*

Sehgal, J., & Ito, S. (1999). Brittleness of glass. *Journal of Non-Crystalline Solids*, *253*(1-3), 126–132.

Sokolnikoff, I. S. (1956). Mathematical theory of elasticity: McGraw-Hill book company.

Xi, X., & Zhong, P. (2001). Dynamic photoelastic study of the transient stress field in solids during shock wave lithotripsy. *The Journal of the Acoustical Society of America*, 109(3), 1226-1239.

Yang, C. *Mechanisms of Stone Fragmentation Produced by Nano Pulse Lithotripsy.* 2017. Duke U, PhD dissertation.

Yuce, H.H., Nelson, D.V., Resch, M.T. (1985). The use of surface acoustic waves to study small fatigue cracks in 7075-T651 aluminumand 4340 steel, In: Thompson, D.O., Chimenti,

Zhang, Y., Yang, C., Qiang, H., & Zhong, P. (2019). Nanosecond shock wave-induced surface acoustic waves and dynamic fracture at fluid-solid boundaries. *Physical Review Research*, 1(3), 033068.

Zhang, Y. *Nanosecond Shock Wave-Induced Surface Acoustic Waves and Fracture at Fluid-Solid.* 2018. Duke U, PhD dissertation.

Zhong, P., Chuong, C., & Preminger, G. (1993). Characterization of fracture toughness of renal calculi using a microindentation technique. *Journal of materials science letters, 12*(18), 1460-1462.

Zhong, P., Shock wave lithotripsy, in Bubble dynamics and shock waves. 2013, *Springer*. p. 291-338.

Zhu, S., Cocks, F. H., Preminger, G. M., & Zhong, P. (2002). The role of stress waves and cavitation in stone comminution in shock wave lithotripsy. *Ultrasound in medicine & biology*, 28(5), 661-671.

Zhu, J., & Popovics, J. S. (2006). Analytical study of excitation and measurement of fluid-solid interface waves. *Geophysical research letters*, *33*(9).